
MULTIMODAL MRI-BASED DETECTION OF AMYLOID STATUS IN ALZHEIMER'S DISEASE CONTINUUM

Giorgio Dolci^{1,2,3}, Charles A. Ellis³, Federica Cruciani², Lorenza Brusini², Anees Abrol³,
 Ilaria Boscolo Galazzo², Gloria Menegaz^{2,+}, and Vince D. Calhoun^{3,+},
 for the Alzheimer's Disease Neuroimaging Initiative*

¹Department of Computer Science, University of Verona, Verona, Italy

²Department of Engineering for Innovation Medicine, University of Verona, Verona, Italy

³Tri-Institutional Center for Translational Research in Neuroimaging and Data Science (TReNDS),
 Georgia State University, Georgia Institute of Technology, Emory University, Atlanta, GA, USA

+V.D. Calhoun and G. Menegaz equally contributed as last authors to this work.

*Data used in preparation of this article were obtained from the Alzheimer's Disease Neuroimaging Initiative (ADNI) database (adni.loni.usc.edu). As such, the investigators within the ADNI contributed to the design and implementation of ADNI and/or provided data but did not participate in analysis or writing of this report. A complete listing of ADNI investigators can be found at:
http://adni.loni.usc.edu/wp-content/uploads/how_to_apply/ADNI_Acknowledgement_List.pdf

June 21, 2024

ABSTRACT

Amyloid- β ($A\beta$) plaques in conjunction with hyperphosphorylated tau proteins in the form of neurofibrillary tangles are the two neuropathological hallmarks of Alzheimer's disease (AD). In particular, the accumulation of $A\beta$ plaques, as evinced by the A/T/N (amyloid/tau/neurodegeneration) framework, marks the initial stage. Thus, the identification of individuals with $A\beta$ positivity could enable early diagnosis and potentially lead to more effective interventions. Deep learning methods relying mainly on amyloid PET images have been employed to this end. However, PET imaging has some disadvantages, including the need of radiotracers and expensive acquisitions. Hence, in this work, we propose a novel multimodal approach that integrates information from structural, functional, and diffusion MRI data to discriminate $A\beta$ status in the AD continuum. Our method achieved an accuracy of 0.762 ± 0.04 . Furthermore, a *post-hoc* explainability analysis (guided backpropagation) was performed to retrieve the brain regions that most influenced the model predictions. This analysis identified some key regions that were common across modalities, some of which were well-established AD-discriminative biomarkers and related to $A\beta$ deposition, such as the hippocampus, thalamus, precuneus, and cingulate gyrus. Hence, our study demonstrates the potential viability of MRI-based characterization of $A\beta$ status, paving the way for further research in this domain.

1 Introduction

The amyloid cascade hypothesis in Alzheimer's Disease (AD) posits that the accumulation of extracellular Amyloid- β ($A\beta$) neuritic plaques in the brain leads to tauopathy and consequent neurodegeneration ([1]). Hence, $A\beta$ deposition in the brain is considered to be the first step and the principal trigger of AD pathology ([2, 1]). In consequence, neurodegeneration of gray matter (GM) may be related to the deposition of $A\beta$ plaques, resulting in cerebral atrophy and synaptic loss ([3]), altering many brain regions, especially subcortical areas, and functional networks. Additionally, $A\beta$ plaques in AD are also linked with demyelination of white matter (WM) tracts ([4]).

The precise identification of $A\beta$ proteins, and thus the classification of patients as $A\beta$ positive or negative, is only possible through amyloid positron emission tomography (PET) scans and cerebrospinal fluid (CSF) tests. Despite their

undeniable utility, their use has some negative implications. Specifically, amyloid PET uses ionizing radiation and radioactive tracers, is expensive, and is not widely available ([5, 6]). Additionally, the CSF test requires an invasive lumbar puncture.

In contrast, common, non-invasive MRI techniques can help identifying the effects of $A\beta$ plaques in the brain. In particular, structural MRI (sMRI) has been widely used for AD detection and early-prediction due to its ability to detect GM atrophy and structural changes. Resting-state functional MRI (rs-fMRI) detects changes in blood oxygenation level-dependent (BOLD) signals, which depend on neurovascular coupling, and hence indirectly measures brain neural activity ([7]). Different resting-state networks (RSNs), like the saliency and default-mode (DM) networks, are closely related to AD pathology, showing functional alterations ([8, 9, 10]). Finally, diffusion MRI (dMRI) is an imaging technique that relies on the movement of water molecules to mark WM boundaries enabling the reconstruction of fiber trajectories and the study of brain structural connections in AD ([4]). Additionally, dMRI data are used to extract microstructural information ([11]). These two modalities are generally used to map whole-brain connectomes, with rs-fMRI describing the functional connectivity (FC) between regions (usually in terms of correlations) and dMRI the structural connectivity (SC) (most often relying on the number of WM fibers).

Currently, different studies focusing on $A\beta$ classification tasks (positive vs negative) in AD research have employed PET images and related features with deep learning (DL) models, while only a few works used MRI data. [12] considered a slice-level approach for the identification of the $A\beta$ status in conjunction with a 2D-CNN for feature extraction and classification. In the same manner, [13] adopted the slice-level approach for the classification of $A\beta$ status employing two different 2D-CNN (ResNet-50 and ResNet-152). These two works were able to reach a high level of accuracy (around 0.95) using a slice-level method. On the other hand, [6] considered three different well-known 3D-CNNs for detecting $A\beta$ positivity relying on 3D Flortbetaben brain PET images. [14] developed a particular CNN composed of different submodules for analyzing the 3D FDG-PET images, converting them into slices following the three different axes. [15] faced the problem of $A\beta$ classification relying on both early and delay-phase FBB PET images and tested their models considering both single and fused modalities. Using FDG and Amyloid PET-derived images, they were able to reach competitive performance in this task, with accuracies around 0.80. More recently, [16] employed FDG-PET-derived features in order to predict the $A\beta$ status in the AD continuum. To this end, they tested eight different feature selection methods and eight different classifiers. LASSO in conjunction with the Gaussian Naive Bayes (GNB) model performed better with respect to the others, achieving an AUC of 0.924. Regarding MRI-based approaches for $A\beta$ detection, [17] employed sMRI images in conjunction with a 3D-CNN, while [18] used an SDF-based convolutional network to analyze the hippocampus region. Using sMRI-derived images and features, they were able to reach accuracies around 0.75. Due to the heterogeneous factors that lead to AD, in recent years, many studies have focused on multimodal DL models due to their ability to integrate information of different nature and to outperform single-modality methods ([19, 17, 20]). Moreover, among the different DL models, graph neural and convolutional networks (GNNs/GCNs) are becoming popular in neuroscience due to their perfect fit to functional and structural brain networks. [21] proposed a benchmark for analyzing fMRI and dMRI networks through GNNs, testing different messages passing, node features, and pooling operations, while Wee and colleagues developed a GCN to study the cortical thickness ([22]).

Although DL models can achieve high performance in different tasks, they do not easily provide interpretable output for what they have learned, which is particularly problematic in clinical and biomedical domains. To address this issue, eXplainable Artificial Intelligence (XAI) methods have been developed allowing to identify the contributions of input features to final predictions potentially highlighting crucial physiological information for AD ([23, 24, 25, 26]).

In this study, we present a multimodal and explainable DL framework for the classification of $A\beta$ positive and negative status in the AD continuum. Our framework included structural and functional connectomes derived from dMRI and rs-fMRI, respectively, along with sMRI-derived GM 3D volumes in order to investigate complementary aspects as well as their relations. This was complemented with an extensive *post-hoc* XAI analysis to uncover the input features that most influenced the final predictions.

2 Methods

2.1 Dataset

The sMRI, rs-fMRI, and dMRI neuroimaging data used in the preparation of this article were obtained from the Alzheimer’s Disease Neuroimaging Initiative (ADNI) database (adni.loni.usc.edu). The ADNI was launched in 2003 as a public-private partnership, led by Principal Investigator Michael W. Weiner, MD. The primary goal of ADNI has been to test whether serial MRI, PET, other biological markers, and clinical and neuropsychological assessment could be combined to measure the progression of mild cognitive impairment (MCI) and early AD. For up-to-date information, please refer to www.adni-info.org.

One of the key strengths of the dataset is the inclusion/exclusion criteria adopted to recruit the subjects; subjects with neurological diseases other than AD and with different substance/drug use were excluded from the study. Due to this, the results we uncover related to $A\beta$ are unlikely to be related to other diseases or the use of a particular substance. For more information about exclusion criteria, please refer to the official document at this link: https://adni.loni.usc.edu/wp-content/themes/freshnews-dev-v2/documents/consentForms/ADNI3_ProtocolVersion3.1_20201204.pdf.

In this work, our dataset was initially composed of 18416 preprocessed sMRI images (from 2144 subjects) from the ADNI 1, 2, 3, and GO phases, out of which 18334 passed quality control (QC) (from 2143 subjects). For rs-fMRI, 2584 preprocessed images were considered (from 1143 individuals) from the ADNI 2, 3, and GO phases, out of which 2450 passed QC (from 1105 individuals). For dMRI, 901 preprocessed images (from 901 subjects) from ADNI 3 were considered, out of which 894 (from 894 subjects) passed QC. Additional information about QC is detailed in the next paragraph. The images of the first available timepoint from only subjects belonging to control (CN), significant memory concern (SMC), early MCI (EMCI), late MCI (LMCI), and AD clinical classes, that had all three modalities, and available $A\beta$ status were included. Lumbar puncture to retrieve CSF samples was performed using the procedures described on the ADNI website, and subjects were labeled as $A\beta$ positive or negative based on the $A\beta$ protein levels reported by the CSF test. Similarly to [5], a cutoff of 980pg/mL was used to define the $A\beta$ status (i.e., < 980 pg/mL for positivity). After that, $A\beta$ negative CN, SMC, and EMCI (69, 75, and 41 subjects, respectively) were considered as 'control class', while $A\beta$ positive EMCI, LMCI, and AD (53, 53, and 27 patients, respectively) formed the 'patient class', resulting in a final cohort of 318 individuals. Table 1 shows the demographic information of the final cohort.

Status	# of subjects	Age	Sex (M/F)	MMSE	$A\beta_{42}$	CN	SMC	EMCI	LMCI	AD
$A\beta$ -	185	71.8 ± 7.1	68/117	28.9 ± 1.5	1684.3 ± 601.2	69	75	41	-	-
$A\beta$ +	133	74.5 ± 7.5	71/62	25.3 ± 4.3	607.5 ± 189.3	-	-	53	53	27

Table 1: Demographic information of the $A\beta$ cohort patients.

The MRI images for the considered cohort were collected as follows: i) T1-weighted sMRI: TR/TE=shortest, TI=900 ms, FOV= 256×256 mm², 1 mm isotropic resolution, slices=176 – 211; ii) rs-fMRI: TR/TE=3000/30 ms, FOV= $220 \times 220 \times 163$ mm³, 3.4 mm isotropic resolution, 200 volumes in almost all subjects, with minimal variations (e.g., 195 – 197) in a small subset; iii) single-shell dMRI: TR/TE=56/7200 ms, FOV= $232 \times 232 \times 160$ mm³, 2 mm isotropic resolution, b=0 and 1000 s/mm².

2.2 Preprocessing and Feature extraction

The sMRI preprocessing included tissue segmentation of GM, WM, and CSF with the modulated normalization algorithm in the statistical parametric mapping toolbox (SPM12, <http://www.fil.ion.ucl.ac.uk/spm/>). This work used GM volumes smoothed with a Gaussian kernel (FWHM=6mm). For QC, images that had a low correlation with individual and/or group-level masks were discarded, which involved correlating data at three levels: the entire image, the top 20 slices, and the bottom 20 slices. The full preprocessed GM volume was input to the sMRI channel of the neural network, resulting in an input size of $121 \times 145 \times 121$ for each subject.

Adhering to the process proposed in [27], the rs-fMRI data was preprocessed with SPM12 including rigid body motion correction, removal of scans with high head motion parameters ($> 3^\circ$ of rotations and > 3 mm in translations), slice-timing correction, warping to the standard MNI space using the EPI template, resampling to 3 mm³ isotropic voxels, and smoothing with a Gaussian kernel (FWHM = 6 mm). QC was the same as for sMRI, correlating the data at three levels: the entire image, the top 5 slices, and the bottom 5 slices. Fifty-three maximally independent components (ICs) covering the whole brain were extracted using spatially constrained ICA with the Neuromark_fmri_1.0 template (available in the GIFT software; <http://trendscenter.org/software/gift>). The ICs were divided into 7 RSNs: the i) Sub-cortical (SuC); ii) Auditory (AU); iii) Sensorimotor (SM); iv) Visual (VI); v) Cognitive-control (CC); vi) DM); and, vii) Cerebellar (CB) networks. For each subject, the Pearson correlation between IC time courses was computed, resulting in a 53x53 static functional network connectivity (FNC) matrix, where FNC is the network analog of FC in that the timecourses represent weighted partially overlapping whole brain patterns. Finally, each FNC matrix was converted into a complete, undirected, and weighted graph. The edges' weights correspond to the FNC correlation values, considering both positive and negative values, while the values of the 53 nodes (i.e., ICs) were initialized at a value of one in order to force the network to learn a latent representation based only on the connectivity information. This FNC-based graph was the input to the rs-fMRI channel.

The dMRI volumes were preprocessed via brain extraction followed by Eddy currents correction (FSL 6.0, <https://fsl.fmrib.ox.ac.uk/>). The data was then denoised using local principal component analysis (PCA) via empirical thresholds relying on the Python *dipy* library. Subsequently, nonlinear registration to the MNI space was applied to correct for EPI-induced currents. QC was performed during preprocessing by visual inspection of images before and after registration. MRtrix 3.0 (<https://www.mrtrix.org/>) was used to derive an anatomically constrained probabilistic tractography (2 million streamlines, step=0.3mm, maximum length=300mm, and backtracking) filtered with SIFT2 ([28]). Subject-specific brain parcellations from T1-weighted images were derived using FreeSurfer (<https://surfer.nmr.mgh.harvard.edu/>) and used as regions of interest (ROIs) in the SC calculation. The SC matrix was built by counting the number of streamlines connecting all pairs of regions from the Desikan-Killiany ([29]) structural atlas, ignoring self-connections. Similarly to rs-fMRI, each SC matrix was converted into a complete, undirected, and weighted graph. In this case, the edges' weights were defined as the number of streamlines between pairs of ROIs, and the values of the 84 nodes (i.e., anatomical ROIs) were initialized to one. This SC-based graph was the input to the dMRI channel.

2.3 Framework architecture

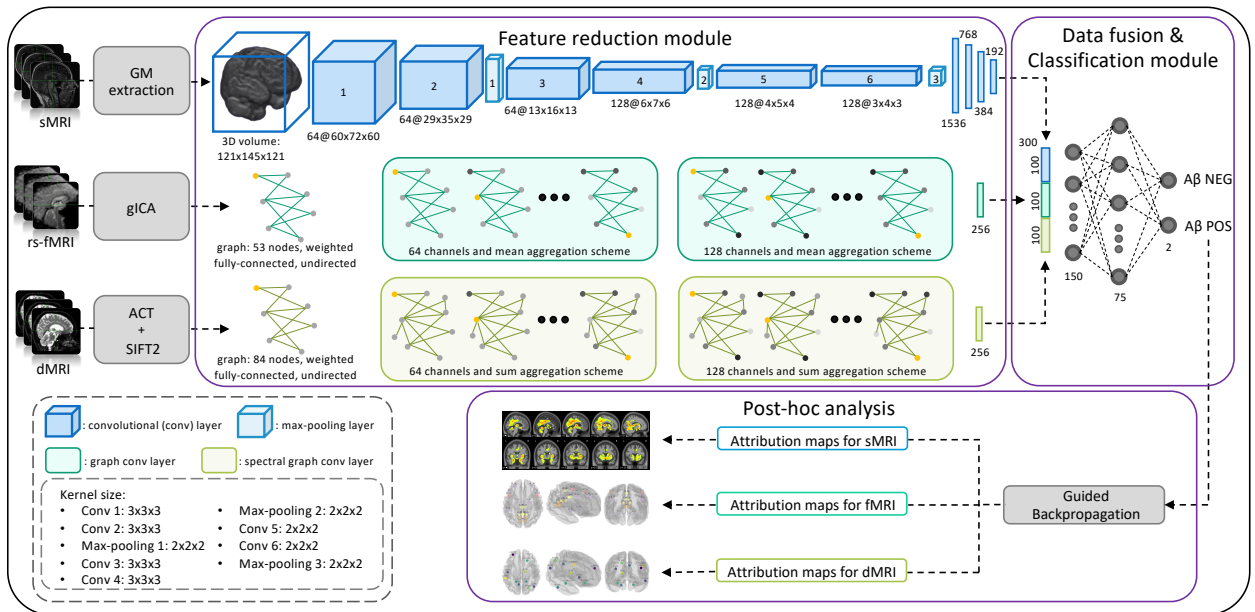


Figure 1: Schematic representation of the proposed framework. The model takes as input three MRI neuroimaging modalities: sMRI 3D volumes, rs-fMRI functional graph, and dMRI structural graph. The DL architecture is composed of two modules: i) a feature reduction module, where the input data are transformed in their latent representations; and ii) a data fusion & Classification module, where the latent feature of each modality are concatenated together and, finally, they are classified using a MLP.

The proposed framework is shown in Figure 1. In detail, the DL architecture used for the classification of $A\beta$ status (positive/negative) has two modules: i) a *feature reduction module* that actuates feature reduction using three different Neural Networks (NNs) to transform the input data into corresponding latent representations; and ii) a *data fusion & classification module* that concatenates the latent representations of each modality and uses a Multilayer Perceptron (MLP) that takes the fused latent features as input for the final classification. Finally, a *post-hoc* explainability analysis was performed on the correctly classified subjects to obtain feature contributions for the classification task. In the following paragraphs, the two modules are further described.

Feature reduction module Three different NNs form the *feature reduction module*. Each NN extracts a latent representation of one modality resulting in a latent vector of 100 features. The 3D sMRI volumes were analyzed using a 3D-CNN with six convolutional layers and three max-pooling layers, completed with four dense layers. Conversely, both FNC and SC graphs were analyzed using two different GCNs. These models update the representation of the node aggregating neighbor information, iteratively in each layer, through the message-passing scheme. The rs-fMRI channel was analyzed using a GCN with two graph convolutional layers proposed by [30] that were followed by a dense layer. This type of convolutional layer is a powerful operator that integrates both high- and low-level structures

along with their relationships into a single graph ([30]). The dMRI channel was analyzed with a different GCN with two Chebyshev spectral graph convolutional layers proposed by [31] and then followed by a dense layer. Spectral convolutional layers are high-performance layers that have been used effectively in irregular graphs ([32]). These two architectures were chosen on an empirical basis as those leading to the best unimodal classification accuracy.

Data fusion & Classification module The *data fusion & classification module* consists of a fusion layer and a classifier. The fusion layer concatenates the latent features extracted from the three channels, resulting in a vector of 300 features that incorporate information from all three modalities for each subject. Lastly, the latent vector was used as input for the final MLP classifier, composed of three dense layers. The convolutional and dense layers in this framework used a ReLU activation function, except for the last layer, which used a softmax activation function to obtain the classification probabilities for each class.

2.4 Training scheme and evaluation

The model was trained with stratified 5-fold cross-validation on the entire cohort to investigate its generalizability across individuals, and a hyperparameter search was performed empirically. The mini-batch strategy (with 16 subjects per batch) was adopted. The Adam optimizer (learning rate: 0.00001) was used to update the entire multimodal architecture. L2 regularization (weight decay: 0.0001) was applied to reduce overfitting. Weighted cross entropy was used as the loss function. The model was trained for 200 epochs.

Performance was evaluated using the mean evaluation accuracy, precision, recall, and F1 score over the five folds.

For comparison, we also tested the unimodal models with the corresponding MRI data, where the architectures were the same of the different branches of the multimodal framework (i.e., 3D-CNN for sMRI, and GCN for both rs-fMRI and dMRI).

3 Post-hoc analysis

3.1 Guided backpropagation

The *post-hoc* XAI analysis was conducted using guided backpropagation (GBP) ([33]). GBP uses the model gradients to extract the feature contribution maps with the same shape as the input data. It belongs to the "modified backpropagation" class of XAI methods in which the backward flow of gradients is modified with ReLU activation ([34]), setting the negative gradients to zero and only allowing non-negative gradients to be backpropagated. This approach enables the visualization of which input features activated the neurons and most contributed to the final prediction.

3.2 Contribution maps and Statistical analysis

The attribution maps were extracted for the correctly classified $A\beta$ positive subjects, and in particular, we focused on the average $A\beta$ positive attribution map to identify the most important features. To evaluate the sMRI GBP contribution maps, the Harvard-Oxford ([29]) and the probabilistic cerebellar ([35]) atlases from FSL were employed to define 56 different ROIs, including cortical, subcortical, and cerebellum regions. The sum of GBP attributions inside each ROI was calculated for the sMRI and weighted to account for the volume of each specific region. Conversely, the GBP attribution of each node for both rs-fMRI and dMRI was extracted directly from the two GCNs. Then, considering the average map for each modality, the percentage of explanation for each region/node was computed over the total contribution within and between each modality. The top 10 ROIs (sMRI) and nodes (rs-fMRI and dMRI) with the highest percentage of GBP contribution were selected for further investigation.

Subsequent statistical analyses were performed on the original data for all correctly classified subjects. For the sMRI, the mean values of the top 10 ROIs resulting from the XAI analysis were extracted from the input GM volumes and used as features for the statistical analysis. For the rs-fMRI and dMRI, graph-based measures were first derived from the full connectivity matrices in order to have a summary measure per node, and then we considered only the top 10 nodes for both rs-fMRI and dMRI for the statistical analysis. In particular, the node strength was computed for rs-fMRI and FNC matrices. This is defined as the sum of the weights of the edges connected with a given node, where in absolute terms, higher values mean more important nodes. Betweenness centrality was calculated for SC matrices, representing the fraction of all shortest paths in the SC matrix that contains the node under analysis, where the shortest path is the shortest sequence of nodes between node i and node j . As the sparsity of the SC matrix could limit the interpretation of the node strength results for the dMRI data, we preferred to rely on a centrality measure for this analysis. In this case, nodes that belong to more paths likely play a pivotal role in the propagation of the information inside the network. These two metrics were computed using the Brain Connectivity Toolbox (BCT) ([36]) in Matlab.

Mann-Whitney tests were then used to compare the values of all these features for the top 10 ROIs/nodes between $A\beta$ positive and negative correctly classified patients. Finally, FDR correction for multiple comparisons was applied to the p -values obtained from the statistical tests.

4 Results

4.1 Classification performance

The proposed framework for the classification of $A\beta$ status achieved a mean \pm std accuracy, precision, recall, and F1 score of 0.762 ± 0.04 , 0.694 ± 0.05 , 0.774 ± 0.10 , and 0.727 ± 0.05 , respectively, across the evaluation folds.

The single networks that composed the multimodal framework along with the corresponding input data were also tested in the same classification task. Table 2 shows the performance comparisons for the multimodal method and the three unimodal models. Results highlight how the multimodal framework is able to outperform the unimodal models in terms of accuracy, recall, and F1 score in the same classification task.

Model	ACC	PRE	REC	F1
Multimodal	0.762 ± 0.04	0.694 ± 0.05	0.774 ± 0.10	0.727 ± 0.05
Unimodal sMRI	0.750 ± 0.06	0.721 ± 0.06	0.672 ± 0.16	0.683 ± 0.09
Unimodal fMRI	0.593 ± 0.05	0.423 ± 0.23	0.303 ± 0.21	0.338 ± 0.19
Unimodal dMRI	0.603 ± 0.04	0.419 ± 0.25	0.311 ± 0.28	0.322 ± 0.23

Table 2: Classification performance of the proposed multimodal framework with respect to the unimodal models for sMRI, rs-fMRI, and dMRI used in the same classification tasks. ACC=accuracy, REC=recall, PRE=precision.

4.2 GBP-based attribution maps

The evaluation set in the fold with the highest evaluation accuracy was used for the *post-hoc* analysis. Importantly, in the analyzed fold, the evaluation subjects were not used for training.

Figure 2A shows the sMRI GBP attribution map for the mean $A\beta$ positive patient overlaid to the MNI template. Qualitatively, mainly subcortical regions (e.g., *hippocampus*, *thalamus*) are relevant to the final classification along with a few cortical areas.

Figure 2B shows the 10 most important nodes for the rs-fMRI modality. All displayed nodes (ICs) are bihemispheric, except for the left inferior parietal lobule (IC38) node, which is mainly in the left hemisphere. The most important nodes belong to the *DM* (3 nodes), *CC* (4 nodes), *VI* (2 nodes), and *SM* (1 node) networks.

Finally, Figure 2C shows the 10 most important dMRI nodes (ROIs). Subcortical regions (*thalamus*, *cerebellum*) along with areas in the *frontal*, *temporal*, and *parietal lobes* are identified.

4.3 Feature relevance & Statistical analysis

Figure 3A shows violinplots for the top 10 sMRI features, while Table 3a shows the corresponding percentages of mean GBP contribution across $A\beta$ positive correctly classified patients for the same regions, weighted by their volumes. The Table also reports the p -values and FDR-corrected p -values of the statistical tests performed on the input features. We identified significant differences between classes after FDR correction in the *precuneus*, *cingulate gyrus* (posterior division), *thalamus*, *hippocampus*, *supracalcarine and intracalcarine cortices*, *amygdala*, and *temporal occipital fusiform cortex* showing an overall comparison direction of $NEG > POS$.

Figure 3B shows violinplots representing the graph node strength for the top 10 rs-fMRI nodes, while Table 3b shows the mean percentages of GBP contribution extracted from the same nodes (ICs) across $A\beta$ positive patients. After FDR correction, the *precuneus* (IC48) was the only region with significant differences ($NEG < POS$). Before correction, another *precuneus* component (IC43) and *precentral gyrus* (IC14) were also significant with $NEG < POS$, while the *left inferior parietal lobule* (IC38) exhibited a trend towards uncorrected statistical significance ($p < 0.10$, with $NEG < POS$).

Figure 3C shows violinplots representing the graph betweenness centrality for the top 10 dMRI nodes, and Table 3c shows the mean percentages of GBP contribution for the same nodes across $A\beta$ positive correctly classified patients. The *precuneus LH* and *cerebellum RH* were significant when considering uncorrected p -values ($NEG < POS$), but none of the results survived multiple comparison corrections. Moreover, the *right superior parietal gyrus* showed a trend towards significance ($p = 0.07825$, $NEG < POS$).

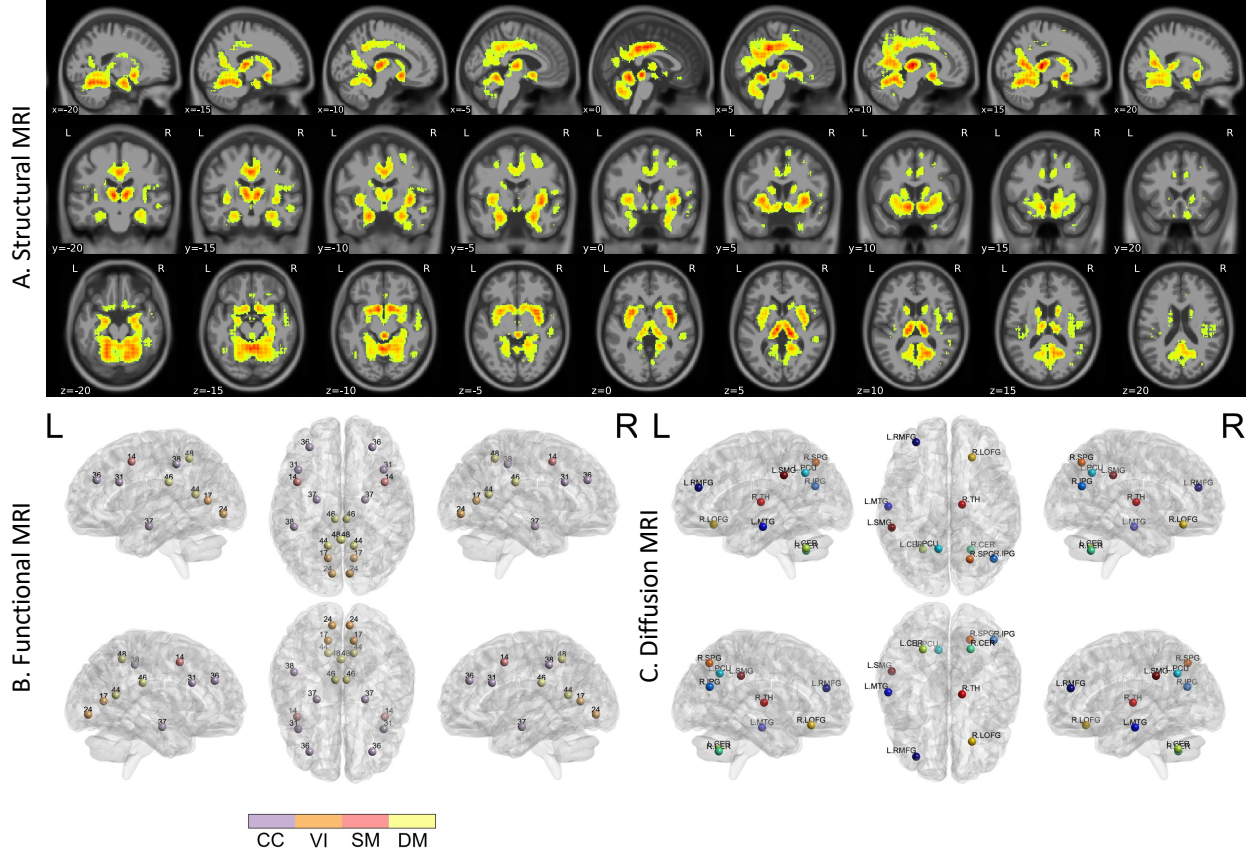


Figure 2: GBP-based attributions for the average $A\beta$ positive patient derived from the correctly classified subjects overlaid to the MNI152 template, where: A. Sagittal, coronal, and axial views for the average sMRI GBP map where only the attributions exceeding the 96th percentile are shown, highlighting both cortical and subcortical regions; B. The 10 most important nodes (ICs) from the rs-fMRI data, representing mainly the DM and CC brain networks; C. The 10 most important nodes (ROIs) from the dMRI data, involving both cortical and subcortical regions in both hemispheres, also including the cerebellum.

We also computed the percentage of contribution of each region for the three modalities combined, and we retrieved the 10 most important areas (marked with [†] in Table 3a,b,c). All the 10 most important brain regions belonged to the sMRI modality (Table 3a).

5 Discussion

In this work, we presented a multimodal data fusion framework that integrates multiple MRI techniques (sMRI, rs-fMRI, and dMRI) for the classification of $A\beta$ status. A *post-hoc* XAI analysis and evaluation was performed using GBP to identify feature importance, complemented by statistical analyses on the identified input features for validation via *post-hoc* plausibility assessment. The underlying assumption is that maximally contributing regions would bring discriminative information across the target classes.

5.1 Classification performance

Our results showed that the multimodal framework outperformed single-modality models in terms of classification performance, in particular for rs-fMRI and dMRI, while the sMRI achieved performance close to the multimodal one, but with high variance across the evaluation folds. This confirms the added value provided by multimodality approaches which improve classification accuracy and, at the same time, carry more information, particularly relevant for the study of complex neurodegenerative diseases influenced by multi-domain factors.

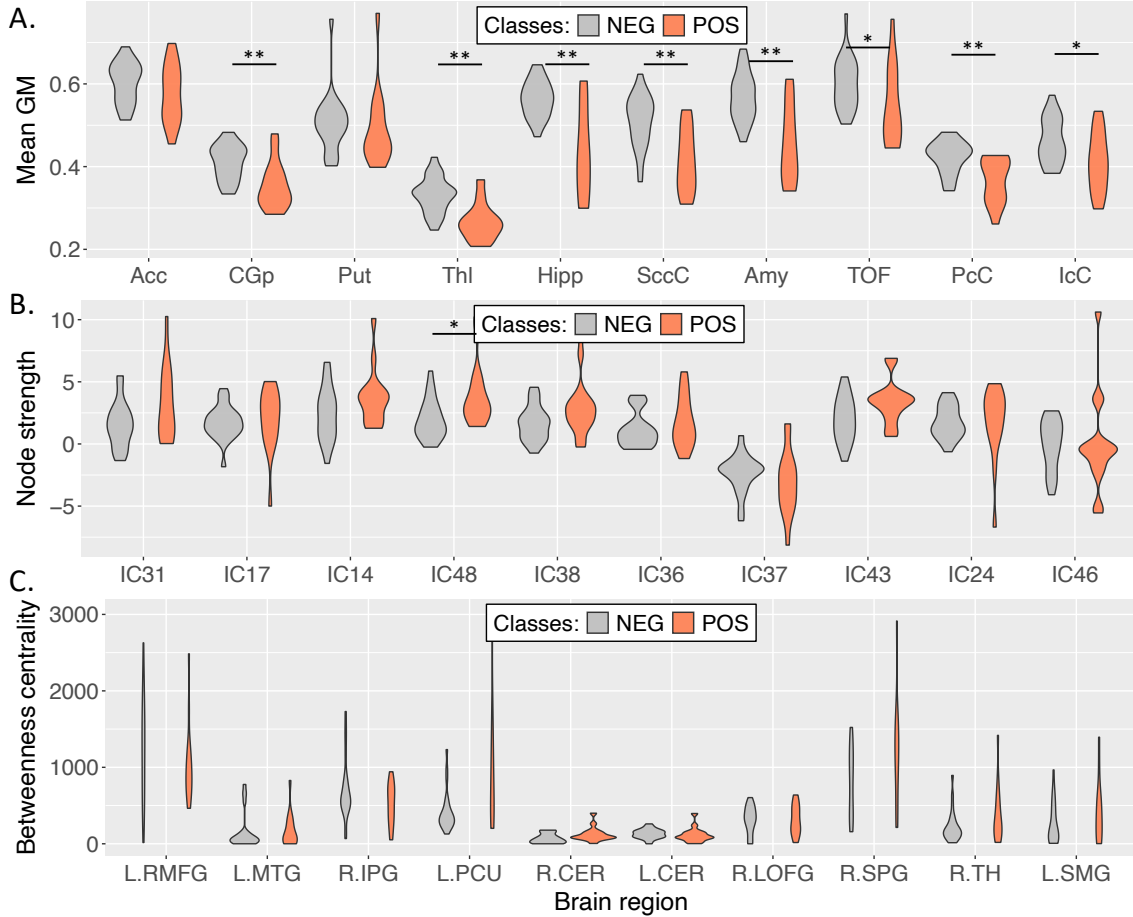


Figure 3: Distributions of the input data for the 10 most important brain regions/nodes considered in the statistical analysis for each modality. A. between-subject distribution of the regional (mean) GM volumes for sMRI; B. between-subject distribution of the node strength values for rs-fMRI; and C. between-subject distribution of the betweenness centrality values for dMRI.

Table 4 shows the performance of state-of-the-art works for the classification of $A\beta$ positive and negative subjects. Of note, current state-of-the-art works use multiple datasets and approaches for addressing this task without considering a common benchmark dataset. Hence, the comparison of the different approaches is imperfect and any resulting conclusions held tentatively. Most of the works relied on PET scans to address this task, e.g., [14] developed a CNN model that takes in input the different views (axial, coronal, and sagittal) of a 3D volume; while [6] used three different well-known 3D-CNN (Inception3D, ResNet3D, and VGG3D) to address this task using the full 3D volume of PET scans as input. They achieved an accuracy of around 0.710 on average in the test set, with a maximum accuracy of 0.870 by [6] using the VGG3D architecture. In the same way, [37] employed a 3D-CNN to identify the $A\beta$ status reporting both the average validation accuracy and also the accuracy on a hold-out test set (ADNI data) using the ensemble method created with the best models across the different folds, achieving accuracies of around 0.980. Recently, [16] employed different combinations of feature selection methods and classifiers in order to analyze FDG-PET-derived features. They achieved an AUC of 0.924 employing LASSO with the GNB model. On the other hand, only few works have used MRI modalities to classify $A\beta$ positive and negative subjects. [18] used only the hippocampus region for predicting $A\beta$ positivity, testing their network on two different classification tasks: AD $A\beta$ POS versus CN $A\beta$ NEG, and MCI $A\beta$ POS versus MCI $A\beta$ NEG. They achieved an accuracy of 0.772 ± 0.03 and 0.592 ± 0.05 , in the first and second tasks, respectively. Lastly, [17] implemented a 3D-CNN for detecting $A\beta$ status from sMRI images defining the $A\beta$ status of the CN, MCI, and AD patients considering the PET cortical standardized uptake value ratio. They achieved an accuracy of 0.760.

Comparing our proposed method with these five works, we outperformed the method that relied on 3D FDG-PET proposed by [14] and the performance of [17]. Our study achieved competitive performance in the validation set

a) Structural MRI

Region	Percentage (%)	p-value	FDR adj. p-value	Comparison direction
Accumbens [†] (Acc)	6.59%	0.20402	0.22669	n.s.
Cingulate gyrus, posterior [†] (CGp)	4.91%	0.00182	0.00304	NEG>POS
Putamen [†] (Put)	4.59%	0.26024	0.26024	n.s.
Thalamus [†] (Thl)	4.09%	0.00016	0.00146	NEG>POS
Hippocampus [†] (Hipp)	3.95%	0.00073	0.00146	NEG>POS
Supracalcarine cortex [†] (ScC)	3.81%	0.00043	0.00146	NEG>POS
Amygdala [†] (Amy)	3.45%	0.00066	0.00146	NEG>POS
Temporal occipital fusiform cortex [†] (TOF)	3.22%	0.01793	0.02561	NEG>POS
Precuneus cortex [†] (PcC)	3.07%	0.00066	0.00146	NEG>POS
Intracalcarine cortex [†] (IcC)	2.83%	0.03509	0.04386	NEG>POS

b) Resting-state functional MRI

Region	RSN	Percentage (%)	p-value	FDR adj. p-value	Comparison direction
Middle frontal gyrus* (IC31)	CC	9.58%	0.10597	0.21194	NEG<POS
Calcarine gyrus (IC17)	VI	6.79%	0.34078	0.42597	n.s.
Precentral gyrus (IC14)	SM	6.31%	0.04965	0.16549	NEG<POS
Precuneus* (IC48)	DM	6.08%	0.00389	0.03892	NEG<POS
Left inferior parietal lobule (IC38)	CC	4.20%	0.07349	0.18372	NEG<POS
Middle frontal gyrus* (IC36)	CC	4.01%	0.32634	0.42597	n.s.
Hippocampus (IC37)	CC	3.76%	0.23658	0.38431	n.s.
Precuneus* (IC43)	DM	3.65%	0.02623	0.13115	NEG<POS
Lingual gyrus (IC24)	VI	3.23%	0.38648	0.42942	n.s.
Posterior cingulate cortex (IC46)	DM	2.94%	0.50672	0.50672	n.s.

c) Diffusion MRI

Region	Percentage (%)	p-value	FDR adj. p-value	Comparison direction
Rostral middle frontal LH (L.RMFG)	39.14%	0.35559	0.44448	n.s.
Middle temporal LH (L.MTG)	9.28%	0.49705	0.55227	n.s.
Inferior parietal RH (R.IPG)	6.55%	0.20919	0.34865	n.s.
Precuneus LH (L.PCU)	5.46%	0.01470	0.14700	NEG<POS
Cerebellum RH (R.CER)	4.48%	0.03887	0.19433	NEG<POS
Cerebellum LH (L.CER)	3.94%	0.14061	0.28187	n.s.
Lateral orbito frontal RH (R.LOFG)	3.78%	0.96545	0.96545	n.s.
Superior parietal RH (R.SPG)	3.76%	0.07825	0.26084	NEG<POS
Thalamus RH (R.TH)	3.30%	0.14094	0.28187	n.s.
Supra marginal LH (L.SMG)	3.29%	0.31926	0.44448	n.s.

Table 3: Percentages of GBP explanations (for the average $A\beta$ positive patient) and the results from the statistical tests for the top 10 brain regions retrieved from: a) sMRI, b) rs-fMRI, and c) dMRI.

The term n.s. means not statistically significant, the sign [†] means top 10 regions across the three modalities, while the sign * means ICs with different spatial locations in rs-fMRI, and LH/RH means left/right hemisphere, respectively, in dMRI.

compared to [6] using amyloid PET images, although our framework achieved a higher accuracy compared to the ResNet3D they used, and a similar accuracy to the one reached by the model proposed by [18] using the hippocampus region only. While the current classification of $A\beta$ positive or negative subjects can only be performed through CSF tests or amyloid PET scans with high precision, the development of different approaches based on non-invasive MRI modalities for determining $A\beta$ status could improve patient care highlighting specific mechanisms that underlie AD. We further showed the ability of our model to successfully integrate structural GM features extracted from a 3D-CNN along with functional and structural connectivity analyzed by two types of GCNs. Notably, while a few studies have recently started to explore SC/FC in conjunction with GCNs in the AD classification tasks ([38, 39]), results are still limited in this specific problem calling for further investigation in the AD continuum.

5.2 Explainability analysis

The *post-hoc* analysis, performed on the correctly classified subjects, consisted of two steps: i) extraction of GBP attribution maps for $A\beta$ positive patients and corresponding percentage of contribution for each brain region both within and between modalities for the average positive patient; ii) statistical analysis on the input features of the 10 most important regions/nodes identified by GBP.

In our analysis of sMRI attribution maps, multiple brain regions involved in AD neurodegeneration were identified. These regions had a higher percentage of contribution relative to the others. These regions belonged to subcortical areas (hippocampus, thalamus, putamen, accumbens, and amygdala) and temporal/occipital/parietal areas (posterior cingulate gyrus, precuneus cortex, supracalcarine and intracalcarine cortices, and the temporal occipital fusiform cortex). The hippocampus, in particular, is a well-known biomarker for AD that is subject to high levels of atrophy. Some studies have suggested that this atrophy is attributable to the deposition of $A\beta$ plaques ([40]). An important region that is connected with the hippocampus is the cingulate gyrus which showed a strong reduction of GM in AD patients ([41, 42]). In a clinical study performed by [43], significant associations were detected between $A\beta$ accumulation and GM atrophy in the hippocampus and posterior cingulate gyrus for the MCI and AD $A\beta+$ patients. Moreover,

Authors	Modalities	Study cohort	Input data	Model	ACC	REC	PRE	F1
[14]	A β /FDG-PET	738 POS, 815 NEG	3D FDG-PET	2.5-D CNN	0.733 [*] -0.690 [†]	0.678 [*] -0.768 [†]	n.d.	0.709 [*] -0.712 [†]
[6]	A β PET	350 POS, 333 NEG	3D A β PET	Inception3D ResNet3D VGG3D	0.954 [*] -0.767 [†] 0.920 [*] -0.671 [†] 0.977 [*] -0.870 [†]	0.918 [*] -0.845 [†] 0.918 [*] -0.944 [†] 0.959 [*] -0.831 [†]	n.d.	n.d.
[37]	A β PET	POS, NEG n.d. 1309 + 224	3D A β PET	3D-CNN	0.980 [*] -0.990 [†]	0.980 [*] -0.990 [†]	n.d.	0.980 [*] -0.990 [†]
[16]	FDG-PET	185 POS, 116 NEG	FDG-PET-derived features	LASSO+GNB	0.924 (AUC)	n.d.	n.d.	n.d.
[18]	sMRI	151 AD POS, 232 CN NEG 171 MCI POS, 171 MCI NEG	Hippocampus region	SDF-based NN	¹ 0.772 \pm 0.03 ² 0.592 \pm 0.05	n.d.	n.d.	n.d.
[17]	sMRI	POS, NEG n.d. 459 CN, 67 MCI, 236 AD	3D volume	3D-CNN	0.760 [†]	n.d.	n.d.	0.746
Proposed framework	sMRI, fMRI, dMRI	133 POS, 185 NEG	GM volume FNC graph, SC graph	Multimodal DL model	0.762 \pm 0.04 [*]	0.774 \pm 0.10 [*]	0.694 \pm 0.05 [*]	0.727 \pm 0.05 [*]

Table 4: Comparison of our proposed model with other state-of-the-art works in the classification task of amyloid- β positive (POS) and negative (NEG). ¹=AD A β + vs CN A β -; ²=MCI A β + vs MCI A β -; * =validation set; [†]=test set; n.d.=not declared

other subcortical structures, like the thalamus and putamen, have a high atrophy rate in clinical patients relative to healthy individuals ([44, 43]), probably due to A β deposition. A previous study highlighted an increase in SUVR (derived from florbetapir PET amyloid) in both putamen and thalamus in the preclinical stages of AD ([45]). In the statistical analysis performed on the input GM volumes, significant differences were detected in the hippocampus, posterior cingulate gyrus, amygdala, thalamus, and precuneus, which demonstrated a considerable decrease of GM in the A β positive patients. These findings were consistent with preexisting literature. Additionally, [46] highlighted other regions (that we also found to be relevant) involved in the different phases of A β deposition (i.e., proisocortex, allocortical areas, diencephalic nuclei, and striatum). For the rs-fMRI, the brain regions (ICs) that most contributed to the final classification resided in the DM and CC networks, along with three regions for VI and SM networks (two and one, respectively). The DM network is involved in memory, self-knowledge, and thinking, and it is highly related to AD ([8, 41]) Previous studies also suggested that DMN is associated with A β plaques ([47]). The CC network is associated with selective attention, working memory, and stimulus-response mapping ([48, 49]). The statistical analysis, performed on the node strength values, detected one region with significant differences between the two groups after FDR correction and three regions before (uncorrected p -values). One more region, the left inferior parietal lobule, exhibited a trend toward significance. Specifically, the A β positive class had a significantly increased node strength in the precentral gyrus (IC14, SM network), which was consistent with the findings of [50] and [51]. The precuneus regions (IC43 and IC48, DM network) were also significantly different between groups with increased strength in the positive group. As in other works ([52, 53]), this suggested that the precuneus plays a key role and undergoes pathological changes related to AD. Previous works also identified the posterior DM (the precuneus and posterior cingulate cortex) ([9]) and parts of the CC network (i.e., the middle frontal gyrus and hippocampus) ([54, 55]) as strongly affected by A β deposition. Lastly, in the dMRI channel, GBP identified multiple cortical and subcortical regions as relevant to the final predictions of our model. The cerebellum was also revealed to be important by the model. Of note, the rostral middle frontal gyrus was assigned a high percentage of contribution relative to the other regions. Additionally, the middle temporal gyrus, precuneus, thalamus, and superior parietal regions showed high importance relative to the other 84 regions. After FDR correction, no region had statistically significant group differences in betweenness centrality values. On the other hand, based upon uncorrected p -values, significant differences ($p < 0.05$) were highlighted in the precuneus and cerebellum (right hemisphere), while the superior parietal region was close to significance ($p=0.07825$). Regarding the two nodes with significant uncorrected differences, the precuneus, which is also identified in the rs-fMRI, is an important hub for functional operations because it is highly connected with other regions by both short- and long-range WM fibers ([53]). On the other hand, different studies highlighted how the cerebellum is subject to increase A β deposition in AD pathology ([56, 57]) at different stages (stage 3 in [58] and stage 5 in [46]) relative to normally aged subjects. Widespread structural alterations in WM tracts connecting cortical and subcortical regions in both hemispheres were detected between A β negative CN and positive preclinical AD patients by [59]. Finally, when combining the explanations of all channels, we found that sMRI most contributed to the final prediction. This was expected as we initially assumed that the effects of A β plaques would predominantly impact GM volumes.

5.3 Common regions across modalities

Multiple brain regions were identified as important by GBP across all three channels. Specifically, the *precuneus* was highlighted in all three modalities. It was one of the most interesting regions as it plays a pivotal role in the transmission

of functional information due to the high concentration of WM tracts linking the precuneus with other brain areas. Our finding of decreased patient GM and increased functional node strength for the region could be related to the functional compensation effects of AD and merits further investigation ([52, 53]). Additionally, the *cingulate gyrus (posterior division)*, *calcarine gyrus*, and *hippocampus*, were important in both sMRI and rs-fMRI. Only the *thalamus* was relevant to both sMRI and dMRI, and the *middle frontal gyrus* was the only area important to both rs-fMRI and dMRI. Interestingly, the *middle frontal gyrus* was a region highlighted in both rs-fMRI and dMRI, but not in the sMRI. This further underlines the importance of integrating different (and complementary) modalities to provide a more complete picture of the complex pathological mechanisms.

5.4 Main contributions and outcomes

We proposed a multimodal and explainable neuroimaging DL model for the classification of amyloid- β positive or negative status. The main contribution of this work is a framework that i) successfully integrates volumetric features and connectivity information from sMRI, rs-fMRI, and dMRI data, extracted from one 3D-CNN and two GCNs, respectively, ii) obtains competitive classification performance ($ACC=0.762 \pm 0.04$) relative to the state-of-the-art with the advantage of avoiding amyloid PET, iii) provides insight into the brain regions that most contribute to final model predictions using a GBP-based *post-hoc* analysis. Finally, we evaluated the XAI outcomes by assessing the discriminative power of the selected input features across classes.

With these analyses, we identified multiple brain regions that suffered from the effects of A β plaque deposition, resulting in atrophy, functional changes, and WM changes relative to the control class. Furthermore, the analysis identified common regions across modalities, including the *precuneus*, *hippocampus*, *thalamus*, *cingulate gyrus*, *calcarine gyrus*, and *middle frontal gyrus*, strengthening the evidence of their involvement in this pathological process.

Our findings highlight the utility of MRI for studying the effects of A β deposition and the importance of integrating complementary information to enable a better understanding of the differences related to amyloid status. However, we acknowledge that a main limitation of this work is the limited number of subjects in the dataset having both A β information and all the considered MRI modalities. Further studies are thus needed to evaluate the generalizability of this multimodal framework to larger datasets, also including subjects with opposite A β status (e.g., CN pos).

6 Conclusion

In this work, we presented a multimodal and explainable DL-based framework for the classification of amyloid- β status, exploiting anatomical and connectivity MRI-based information. The application of GBP enabled the identification of the regions most important to the final model predictions, some of which were common across modalities, (e.g., the precuneus, hippocampus, thalamus, cingulate gyrus, calcarine gyrus, and middle frontal gyrus). Our study demonstrates the potential viability of non-invasive MRI-based detection of amyloid- β status involving multimodal data, paving the way for further research in this direction.

Acknowledgments

Data collection and sharing for this project was funded by the Alzheimer’s Disease Neuroimaging Initiative (ADNI) (National Institutes of Health Grant U01 AG024904) and DOD ADNI (Department of Defense award number W81XWH-12-2-0012). ADNI is funded by the National Institute on Aging, the National Institute of Biomedical Imaging and Bioengineering, and through generous contributions from the following: AbbVie, Alzheimer’s Association; Alzheimer’s Drug Discovery Foundation; Araclon Biotech; BioClinica, Inc.; Biogen; Bristol-Myers Squibb Company; CereSpir, Inc.; Cogstate; Eisai Inc.; Elan Pharmaceuticals, Inc.; Eli Lilly and Company; EuroImmun; F. Hoffmann-La Roche Ltd and its affiliated company Genentech, Inc.; Fujirebio; GE Healthcare; IXICO Ltd.; Janssen Alzheimer Immunotherapy Research & Development, LLC.; Johnson & Johnson Pharmaceutical Research & Development LLC.; Lumosity; Lundbeck; Merck & Co., Inc.; Meso Scale Diagnostics, LLC.; NeuroRx Research; Neurotrack Technologies; Novartis Pharmaceuticals Corporation; Pfizer Inc.; Piramal Imaging; Servier; Takeda Pharmaceutical Company; and Transition Therapeutics. The Canadian Institutes of Health Research is providing funds to support ADNI clinical sites in Canada. Private sector contributions are facilitated by the Foundation for the National Institutes of Health (www.fnih.org). The grantee organization is the Northern California Institute for Research and Education, and the study is coordinated by the Alzheimer’s Therapeutic Research Institute at the University of Southern California. ADNI data are disseminated by the Laboratory for Neuro Imaging at the University of Southern California.

This study was funded by NIH grant (RF1AG063153) and NSF Grant (2112455), as well as Fondazione CariVerona (EDIPO project, num. 2018.0855.2019) and MIUR D.M. 737/2021 “AI4Health: empowering neurosciences with eXplainable AI methods”.

CRediT authors contributions statement

Giorgio Dolci: Conceptualization, Data curation, Formal analysis, Investigation, Methodology, Software, Writing - original draft. **Charles A. Ellis:** Methodology, Writing - original draft. **Federica Cruciani:** Methodology, Data curation, Writing - review & editing. **Lorenza Brusini:** Data curation, Writing - review & editing. **Anees Abrol:** Data curation, Writing - review & editing. **Iliaria Boscolo Galazzo:** Investigation, Data curation, Writing - review & editing. **Gloria Menegaz:** Conceptualization, Supervision, Writing - review & editing, Funding acquisition. **Vince D. Calhoun:** Conceptualization, Supervision, Writing - review & editing, Funding acquisition.

Competing Interests

The authors declare that they have no known competing financial interests or personal relationships that could have appeared to influence the work reported in this paper.

Additional information

The data used in this work were collected by ADNI (<https://adni.loni.usc.edu/>), and they are publically available after requested on the ADNI website.

Ethical standard

The data used in this work were acquired by ADNI (<https://adni.loni.usc.edu/>). Information regarding the ethical standard and informed consent of ADNI 3 Protocol are available at the following link on the: https://adni.loni.usc.edu/wp-content/themes/freshnews-dev-v2/documents/clinical/ADNI3_Protocol.pdf.

References

- [1] Christian Haass and Dennis Selkoe. If amyloid drives alzheimer disease, why have anti-amyloid therapies not yet slowed cognitive decline? *PLoS biology*, 20(7):e3001694, 2022.
- [2] Marina Fernandez-Alvarez, Mercedes Atienza, and Jose L Cantero. Cortical amyloid-beta burden is associated with changes in intracortical myelin in cognitively normal older adults. *Translational Psychiatry*, 13(1):115, 2023.
- [3] Alberto Serrano-Pozo, Matthew P Frosch, Eliezer Masliah, and Bradley T Hyman. Neuropathological alterations in alzheimer disease. *Cold Spring Harbor perspectives in medicine*, 1(1):a006189, 2011.
- [4] Stella M Sánchez, Bárbara Duarte-Abritta, Carolina Abulafia, Gabriela De Pino, Hernan Bocaccio, Mariana N Castro, Gustavo E Sevlever, Greg A Fonzo, Charles B Nemeroff, Deborah R Gustafson, et al. White matter fiber density abnormalities in cognitively normal adults at risk for late-onset alzheimer’s disease. *Journal of psychiatric research*, 122:79–87, 2020.
- [5] Oskar Hansson, John Seibyl, Erik Stomrud, Henrik Zetterberg, John Q Trojanowski, Tobias Bittner, Valeria Lifke, Veronika Corradini, Udo Eichenlaub, Richard Batrla, et al. Csf biomarkers of alzheimer’s disease concord with amyloid- β pet and predict clinical progression: a study of fully automated immunoassays in biofinder and adni cohorts. *Alzheimer’s & dementia*, 14(11):1470–1481, 2018.
- [6] Seung-Yeon Lee, Hyeon Kang, Jong-Hun Jeong, and Do-young Kang. Performance evaluation in [18f] florbetaben brain pet images classification using 3d convolutional neural network. *Plos one*, 16(10):e0258214, 2021.
- [7] Keith A Johnson, Nick C Fox, Reisa A Sperling, and William E Klunk. Brain imaging in alzheimer disease. *Cold Spring Harbor perspectives in medicine*, 2(4):a006213, 2012.
- [8] Lorenzo Pini, Alexandra M Wennberg, Alessandro Salvalaggio, Antonino Vallesi, Michela Pievani, and Maurizio Corbetta. Breakdown of specific functional brain networks in clinical variants of alzheimer’s disease. *Ageing Research Reviews*, 72:101482, 2021.

- [9] Sebastian Palmqvist, Michael Schöll, Olof Strandberg, Niklas Mattsson, Erik Stomrud, Henrik Zetterberg, Kaj Blennow, Susan Landau, William Jagust, and Oskar Hansson. Earliest accumulation of β -amyloid occurs within the default-mode network and concurrently affects brain connectivity. *Nature communications*, 8(1):1214, 2017.
- [10] Juan Zhou, Michael D Greicius, Efstathios D Gennatas, Matthew E Growdon, Jung Y Jang, Gil D Rabinovici, Joel H Kramer, Michael Weiner, Bruce L Miller, and William W Seeley. Divergent network connectivity changes in behavioural variant frontotemporal dementia and alzheimer’s disease. *Brain*, 133(5):1352–1367, 2010.
- [11] Mauro Zucchelli, Lorenza Brusini, C Andrés Méndez, Alessandro Daducci, Cristina Granziera, and Gloria Menegaz. What lies beneath? diffusion eap-based study of brain tissue microstructure. *Medical image analysis*, 32:145–156, 2016.
- [12] Hye Joo Son, Jungsu S Oh, Minyoung Oh, Soo Jong Kim, Jae-Hong Lee, Jee Hoon Roh, and Jae Seung Kim. The clinical feasibility of deep learning-based classification of amyloid pet images in visually equivocal cases. *European journal of nuclear medicine and molecular imaging*, 47:332–341, 2020.
- [13] F Reith, ME Koran, G Davidzon, and G Zaharchuk. Application of deep learning to predict standardized uptake value ratio and amyloid status on 18f-florbetapir pet using adni data. *American Journal of Neuroradiology*, 41(6):980–986, 2020.
- [14] Suhong Kim, Peter Lee, Kyeong Taek Oh, Min Soo Byun, Dahyun Yi, Jun Ho Lee, Yu Kyeong Kim, Byoung Seok Ye, Mi Jin Yun, Dong Young Lee, et al. Deep learning-based amyloid pet positivity classification model in the alzheimer’s disease continuum by using 2-[18f] fdg pet. *EJNMMI research*, 11(1):56, 2021.
- [15] Hyeon Kang and Do-Young Kang. Alzheimer’s disease prediction using attention mechanism with dual-phase 18f-florbetaben images. *Nuclear Medicine and Molecular Imaging*, 57(2):61–72, 2023.
- [16] Ramin Rasi and Albert Guvenis. Predicting amyloid positivity from fdg-pet images using radiomics: A parsimonious model. *Computer Methods and Programs in Biomedicine*, page 108098, 2024.
- [17] Tamoghna Chattopadhyay, Saket S Ozarkar, Ketaki Buwa, Sophia I Thomopoulos, Paul M Thompson, Alzheimer’s Disease Neuroimaging Initiative, et al. Predicting brain amyloid positivity from t1 weighted brain mri and mri-derived gray matter, white matter and csf maps using transfer learning on 3d cnns. *bioRxiv*, 2023.
- [18] Zhangsihao Yang, Jianfeng Wu, Paul M Thompson, and Yalin Wang. Deep learning on sdf for classifying brain biomarkers. In *2021 43rd Annual International Conference of the IEEE Engineering in Medicine & Biology Society (EMBC)*, pages 1051–1054. IEEE, 2021.
- [19] G Dolci, MA Rahaman, I Boscolo Galazzo, F Cruciani, A Abrol, J Chen, Z Fu, K Duan, G Menegaz, and VD Calhoun. Deep generative transfer learning predicts conversion to alzheimer’s disease from neuroimaging genomics data. In *2023 IEEE International Conference on Acoustics, Speech, and Signal Processing Workshops (ICASSPW)*, pages 1–5. IEEE, 2023.
- [20] Anees Abrol, Zening Fu, Yuhui Du, and Vince D Calhoun. Multimodal data fusion of deep learning and dynamic functional connectivity features to predict alzheimer’s disease progression. In *2019 41st Annual International Conference of the IEEE Engineering in Medicine and Biology Society (EMBC)*, pages 4409–4413. IEEE, 2019.
- [21] Hejie Cui, Wei Dai, Yanqiao Zhu, Xuan Kan, Antonio Aodong Chen Gu, Joshua Lukemire, Liang Zhan, Lifang He, Ying Guo, and Carl Yang. Braingb: A benchmark for brain network analysis with graph neural networks. *IEEE transactions on medical imaging*, 42(2):493–506, 2022.
- [22] Chong-Yaw Wee, Chaoqiang Liu, Annie Lee, Joann S Poh, Hui Ji, Anqi Qiu, Alzheimers Disease Neuroimage Initiative, et al. Cortical graph neural network for ad and mci diagnosis and transfer learning across populations. *NeuroImage: Clinical*, 23:101929, 2019.
- [23] Anees Abrol, Manish Bhattarai, Alex Fedorov, Yuhui Du, Sergey Plis, Vince Calhoun, Alzheimer’s Disease Neuroimaging Initiative, et al. Deep residual learning for neuroimaging: an application to predict progression to alzheimer’s disease. *Journal of neuroscience methods*, 339:108701, 2020.
- [24] Anees Abrol, Zening Fu, Mustafa Salman, Rogers Silva, Yuhui Du, Sergey Plis, and Vince Calhoun. Deep learning encodes robust discriminative neuroimaging representations to outperform standard machine learning. *Nature communications*, 12(1):353, 2021.
- [25] Moritz Böhle, Fabian Eitel, Martin Weygandt, and Kerstin Ritter. Layer-wise relevance propagation for explaining deep neural network decisions in mri-based alzheimer’s disease classification. *Frontiers in aging neuroscience*, 11:194, 2019.
- [26] Shaker El-Sappagh, Jose M Alonso, SM Riazul Islam, Ahmad M Sultan, and Kyung Sup Kwak. A multilayer multimodal detection and prediction model based on explainable artificial intelligence for alzheimer’s disease. *Scientific reports*, 11(1):2660, 2021.

- [27] Yuhui Du, Zening Fu, Jing Sui, Shuang Gao, Ying Xing, Dongdong Lin, Mustafa Salman, Anees Abrol, Md Abdur Rahaman, Jiayu Chen, et al. Neuromark: An automated and adaptive ica based pipeline to identify reproducible fmri markers of brain disorders. *NeuroImage: Clinical*, 28:102375, 2020.
- [28] Robert E Smith, Jacques-Donald Tournier, Fernando Calamante, and Alan Connelly. Sift2: Enabling dense quantitative assessment of brain white matter connectivity using streamlines tractography. *Neuroimage*, 119:338–351, 2015.
- [29] Rahul S Desikan, Florent Ségonne, Bruce Fischl, Brian T Quinn, Bradford C Dickerson, Deborah Blacker, Randy L Buckner, Anders M Dale, R Paul Maguire, Bradley T Hyman, et al. An automated labeling system for subdividing the human cerebral cortex on mri scans into gyral based regions of interest. *Neuroimage*, 31(3):968–980, 2006.
- [30] Christopher Morris, Martin Ritzert, Matthias Fey, William L Hamilton, Jan Eric Lenssen, Gaurav Rattan, and Martin Grohe. Weisfeiler and leman go neural: Higher-order graph neural networks. In *Proceedings of the AAAI conference on artificial intelligence*, volume 33, pages 4602–4609, 2019.
- [31] Michaël Defferrard, Xavier Bresson, and Pierre Vandergheynst. Convolutional neural networks on graphs with fast localized spectral filtering. *Advances in neural information processing systems*, 29, 2016.
- [32] Sarah Parisot, Sofia Ira Ktena, Enzo Ferrante, Matthew Lee, Ricardo Guerrero, Ben Glocker, and Daniel Rueckert. Disease prediction using graph convolutional networks: application to autism spectrum disorder and alzheimer’s disease. *Medical image analysis*, 48:117–130, 2018.
- [33] Jost Tobias Springenberg, Alexey Dosovitskiy, Thomas Brox, and Martin Riedmiller. Striving for simplicity: The all convolutional net. *arXiv preprint arXiv:1412.6806*, 2014.
- [34] Md Mahfuzur Rahman, Vince D Calhoun, and Sergey M Plis. Looking deeper into interpretable deep learning in neuroimaging: a comprehensive survey. *arXiv preprint arXiv:2307.09615*, 2023.
- [35] Jörn Diedrichsen, Joshua H Balsters, Jonathan Flavell, Emma Cussans, and Narender Ramnani. A probabilistic mr atlas of the human cerebellum. *neuroimage*, 46(1):39–46, 2009.
- [36] Mikail Rubinov and Olaf Sporns. Complex network measures of brain connectivity: uses and interpretations. *Neuroimage*, 52(3):1059–1069, 2010.
- [37] Claes Nøhr Ladefoged, Lasse Anderberg, Karine Madsen, Otto Mølby Henriksen, Steen Gregers Hasselbalch, Flemming Littrup Andersen, Liselotte Højgaard, Ian Law, and Alzheimer’s Disease Neuroimaging Initiative. Estimation of brain amyloid accumulation using deep learning in clinical [11c] pib pet imaging. *EJNMMI physics*, 10(1):44, 2023.
- [38] Yanteng Zhang, Xiaohai He, Yi Hao Chan, Qizhi Teng, and Jagath C Rajapakse. Multi-modal graph neural network for early diagnosis of alzheimer’s disease from smri and pet scans. *Computers in Biology and Medicine*, 164:107328, 2023.
- [39] Jin Zhang, Xiaohai He, Linbo Qing, Xiang Chen, Yan Liu, and Honggang Chen. Multi-relation graph convolutional network for alzheimer’s disease diagnosis using structural mri. *Knowledge-Based Systems*, 270:110546, 2023.
- [40] Jose L Cantero, Juan E Iglesias, Koen Van Leemput, and Mercedes Atienza. Regional hippocampal atrophy and higher levels of plasma amyloid-beta are associated with subjective memory complaints in nondemented elderly subjects. *Journals of Gerontology Series A: Biomedical Sciences and Medical Sciences*, 71(9):1210–1215, 2016.
- [41] Zachary D Green, Eric D Vidoni, Russell H Swerdlow, Jeffrey M Burns, Jill K Morris, and Robyn A Honea. Increased functional connectivity of the precuneus in individuals with a family history of alzheimer’s disease. *Journal of Alzheimer’s Disease*, (Preprint):1–13, 2023.
- [42] Bethany F Jones, Josephine Barnes, Harry BM Uylings, Nick C Fox, Chris Frost, Menno P Witter, and Philip Scheltens. Differential regional atrophy of the cingulate gyrus in alzheimer disease: a volumetric mri study. *Cerebral cortex*, 16(12):1701–1708, 2006.
- [43] Min Su Kang, Arturo Aliaga Aliaga, Monica Shin, Sulantha Mathotaarachchi, Andrea L Benedet, Tharick A Pascoal, Joseph Therriault, Mira Chamoun, Melissa Savard, Gabriel A Devenyi, et al. Amyloid-beta modulates the association between neurofilament light chain and brain atrophy in alzheimer’s disease. *Molecular Psychiatry*, 26(10):5989–6001, 2021.
- [44] Laura W de Jong, Karin van der Hiele, Ilya M Veer, JJ Houwing, RGJ Westendorp, ELEM Bollen, Paul W de Bruin, HAM Middelkoop, Mark A van Buchem, and Jeroen van der Grond. Strongly reduced volumes of putamen and thalamus in alzheimer’s disease: an mri study. *Brain*, 131(12):3277–3285, 2008.
- [45] Emily C Edmonds, Katherine J Bangen, Lisa Delano-Wood, Daniel A Nation, Ansgar J Furst, David P Salmon, Mark W Bondi, Alzheimer’s Disease Neuroimaging Initiative, et al. Patterns of cortical and subcortical amyloid burden across stages of preclinical alzheimer’s disease. *Journal of the International Neuropsychological Society*, 22(10):978–990, 2016.

- [46] Dietmar R Thal, Udo Rüb, Mario Orantes, and Heiko Braak. Phases of $a\beta$ -deposition in the human brain and its relevance for the development of ad. *Neurology*, 58(12):1791–1800, 2002.
- [47] Paul M Matthews, Nicola Filippini, and Gwenaëlle Douaud. Brain structural and functional connectivity and the progression of neuropathology in alzheimer’s disease. *Journal of Alzheimer’s Disease*, 33(s1):S163–S172, 2013.
- [48] Mohammad SE Sendi, Elaheh Zendehtrouh, Zening Fu, Jingyu Liu, Yuhui Du, Elizabeth Mormino, David H Salat, Vince D Calhoun, and Robyn L Miller. Disrupted dynamic functional network connectivity among cognitive control networks in the progression of alzheimer’s disease. *Brain Connectivity*, 13(6):334–343, 2023.
- [49] Earl K Miller. The prefrontal cortex and cognitive control. *Nature reviews neuroscience*, 1(1):59–65, 2000.
- [50] Edmarie Guzmán-Vélez, Ibai Diez, Dorothee Schoemaker, Enmanuelle Pardilla-Delgado, Clara Vila-Castelar, Joshua T Fox-Fuller, Ana Baena, Reisa A Sperling, Keith A Johnson, Francisco Lopera, et al. Amyloid- β and tau pathologies relate to distinctive brain dysconnectomics in preclinical autosomal-dominant alzheimer’s disease. *Proceedings of the National Academy of Sciences*, 119(15):e2113641119, 2022.
- [51] Huoqiang Duan, Jiehui Jiang, Jun Xu, Hucheng Zhou, Zhemin Huang, Zhihua Yu, Zhuangzhi Yan, Alzheimer’s Disease Neuroimaging Initiative, et al. Differences in $a\beta$ brain networks in alzheimer’s disease and healthy controls. *Brain Research*, 1655:77–89, 2017.
- [52] Kim A Celone, Vince D Calhoun, Bradford C Dickerson, Alireza Atri, Elizabeth F Chua, Saul L Miller, Kristina DePeau, Doreen M Rentz, Dennis J Selkoe, Deborah Blacker, et al. Alterations in memory networks in mild cognitive impairment and alzheimer’s disease: an independent component analysis. *Journal of Neuroscience*, 26(40):10222–10231, 2006.
- [53] Nicholas B Dадario and Michael E Sughrue. The functional role of the precuneus. *Brain*, 146(9):3598–3607, 2023.
- [54] Leonides Canuet, Sandra Pusil, María Eugenia López, Ricardo Bajo, José Ángel Pineda-Pardo, Pablo Cuesta, Gerardo Gálvez, José María Gaztelu, Daniel Lourido, Guillermo García-Ribas, et al. Network disruption and cerebrospinal fluid amyloid-beta and phospho-tau levels in mild cognitive impairment. *Journal of Neuroscience*, 35(28):10325–10330, 2015.
- [55] Joana B Pereira, Rik Ossenkoppele, Sebastian Palmqvist, Tor Olof Strandberg, Ruben Smith, Eric Westman, and Oskar Hansson. Amyloid and tau accumulate across distinct spatial networks and are differentially associated with brain connectivity. *Elife*, 8:e50830, 2019.
- [56] Heiko Braak, Eva Braak, Jürgen Bohl, and Walter Lang. Alzheimer’s disease: amyloid plaques in the cerebellum. *Journal of the neurological sciences*, 93(2-3):277–287, 1989.
- [57] Ana M Catafau, Santiago Bullich, John P Seibyl, Henryk Barthel, Bernardino Ghetti, James Leverenz, James W Ironside, Walter J Schulz-Schaeffer, Anja Hoffmann, and Osama Sabri. Cerebellar amyloid- β plaques: How frequent are they, and do they influence 18f-florbetaben suv ratios? *Journal of Nuclear Medicine*, 57(11):1740–1745, 2016.
- [58] H Braak and E Braak. Evolution of neuronal changes in the course of alzheimer’s disease. *Ageing and dementia*, pages 127–140, 1998.
- [59] José Luis Molinuevo, Pablo Ripolles, Marta Simó, Albert Lladó, Jaume Olives, Mircea Balasa, Anna Antonell, Antoni Rodríguez-Fornells, and Lorena Rami. White matter changes in preclinical alzheimer’s disease: a magnetic resonance imaging-diffusion tensor imaging study on cognitively normal older people with positive amyloid β protein 42 levels. *Neurobiology of aging*, 35(12):2671–2680, 2014.